nature communications

Article

https://doi.org/10.1038/s41467-025-58425-x

Spatiotemporal molecular tracing of ultralow-volume biofluids via a soft skin-adaptive optical monolithic patch sensor

Received: 5 August 2024

Accepted: 18 March 2025

Published online: 05 April 2025

Check for updates

Yeon Soo Lee[1,5], Seyoung Shin[1,5], Gyun Ro Kang[1], Siyeon Lee[1], Da Wan Kim[2], Seongcheol Park[1], Youngwook Cho[1], Dohyun Lim[1], Seung Hwan Jeon[1,3], Soo-Yeon Cho[1,6] ✉ & Changhyun Pang[1,4,6] ✉

Molecular tracing of extremely low amounts of biofluids is vital for precise diagnostic analysis. Although optical nanosensors for real-time spatiotemporal molecular tracing exist, integrating them into simple devices that capture low-volume fluids on rough, dynamic surfaces remains challenging. We present a bioinspired 3D microstructured patch monolithically integrated with optical nanosensors (3D MIN) for real-time, multivariate molecular tracing of ultralow-volume fluids. Inspired by tree frog toe pads, the 3D MIN features soft, hexagonally aligned pillars and microchannels for conformal adhesion and targeted fluid management. Embedding near-infrared fluorescent single-walled carbon nanotube nanosensors in a hydrogel enables simultaneous fluid capture and detection. Softening the elastomer microarchitecture and optimizing water management promote stable adhesion on wet biosurfaces, allowing rapid collection of ultralow-volume fluids (~0.1 μL/min·cm^2). We demonstrate real-time, remote sweat analysis with ≥75 nL volumes collected in 45 s, without exercise or iontophoresis, showcasing high biocompatibility and efficient spatiotemporal molecular tracing.

Tracing chemical and biological molecules such as ions, small molecules, nucleic acids, lipids, and proteins is the key to noninvasive assessment of health status, chemical balance, disease detection, and the monitoring of essential chemical species[1–4]. These analytes vary widely in size, concentration, and volume, making microfluid management important for tracking these molecules from diverse sources and dynamically complex biosurfaces. For example, protein synthesis and secretion occur in irregular patterns, whereas cortisol levels fluctuate with circadian rhythms, adding to analytical complexity[5,6]. For effective molecular tracing, sensitive and selective sensors capable of extracting samples from dynamic sources in appropriate quantities and flow rates are needed. Tracing low-volume analytes, particularly at the nanoscale to the microliter scale, is valuable for precision medicine, early diagnostics, and trace chemical production[7,8]. Traditional methods such as mass spectrometry and chromatography are accurate, but the equipment involved is too large and complex for the real-time analysis of low-volume samples, which quickly dissipate due to evaporation[9–11]. Nanosensors with molecular recognition capacity serve as promising alternatives in which optical, electrical, or mechanical properties are used to obtain real-time signals. In particular, optical nanosensors consisting of quantum dots (QDs), carbon dots, and single-walled carbon nanotubes (SWCNTs) can provide molecular information even at the single-molecular level through fluorescence or absorption variations with increasing molecular

[1]School of Chemical Engineering, Sungkyunkwan University (SKKU), Suwon, Republic of Korea. [2]Department of Electronic Engineering, Korea National University of Transportation, Chungju-si, Chungbuk, Republic of Korea. [3]Convergence Research Center for Meta-Touch, Korea Research Institute of Standards and Science, Daejeon, Republic of Korea. [4]Samsung Advanced Institute for Health Sciences and Technology (SAIHST), Sungkyunkwan University, Suwon, Republic of Korea. [5]These authors contributed equally: Yeon Soo Lee, Seyoung Shin. [6]These authors jointly supervised this work: Soo-Yeon Cho, Changhyun Pang. ✉e-mail: sooyeonc@skku.edu; chpang@skku.edu

adsorption[12–15]. However, when these sensors are integrated into bulky devices, their capacity to analyze samples with varying volumes and fluid rates becomes limited. To address this, tailored nanoprobes must be integrated into a systematically designed 3D interface for efficient sample capture. New analytical components are needed to absorb and measure small amounts of fluid effectively, to ensure stable adhesion through conformal contact and compatibility with biological surfaces to capture irregular secretions of low-volumes of fluid and to enhance both the efficiency and portability of nanosensors.

To date, technologies that involve mounting sensors at the skin interface have been developed to capture and analyze biofluids. To achieve this goal, multilayered components that can capture biofluids have been combined with sensors that distinguish and analyze electronic signals or colors to facilitate effective diagnosis[16–19]. Despite these striking advances, the development of devices that integrate a collection and sensing layer that can rapidly collect and simultaneously detect small amounts of biofluids remains challenging. In addition, the ease of use and economic efficiency of skin-attachable biosensing platforms can be maximized by monolithically fabricating them from a single biofluid capture-sensing layer and developing an adhesive substrate capable of reversible adhesion on human skin without causing irritation.

Here, we address this challenge by developing a 3D microstructured patch integrated with optical nanosensors (3D MIN) that enables real-time, multivariate molecular tracing of extremely low-volume fluids directly from a dynamic source (Fig. 1a). Inspired by the micropatterns on frog toe pads, the hexagonal surfaces, surrounded by microchannels, drain surface fluids into the channels, and the soft layer on the hexagonal surfaces provides stable, conformal adhesion without skin irritation, even on irregular and dynamic biosurfaces. For the optical probe in 3D MIN, we synthesized near-infrared (nIR) fluorescent SWCNT nanosensors with selective molecular recognition capabilities and embedded the sensors in a hydrogel layer monolithically integrated into the drainable channel areas. This integration facilitated the rapid capture of ultralow volumes of fluids at slow flow rates and ensured stable sample collection on rough, dynamic surfaces. By leveraging the selective and sensitive molecular recognition capabilities of the nanosensor array in 3D MIN, we used our patch to perform real-time and remote multivariate and spatiotemporal molecular tracing of biofluids (e.g., health indicators in human sweat).

Results and discussion

Fabrication of 3D MIN inspired by nature

We were inspired by the hexagonal epithelial cells on the toe pads of the tree frog *Rhacophorus pardalis*[20–22]. These pads, while supported by rigid pillars, are covered with a soft material with an elastic modulus of ~25 kPa, which allows them to conform easily to wet and irregular surfaces (Fig. 1b)[21]. By mimicking the functionalities of the tree frog toe pad, we designed a 3D MIN to enhance surface contact on rough and wet surfaces and efficiently drain liquid between interfaces into internal microchannels (Fig. 1c-i). Since the soft adhesive structural substrate and the unified capture-sensing layer were fabricated monolithically, the drained liquids were easily captured by embedded nanosensor-containing hydrogels (nanosensors/hydrogels). The robust adhesion interface had hexagonally aligned 3D microchannels with a soft PDMS (s-PDMS) coating on its surface (Fig. 1c-ii). The target liquid at the interface was effectively drained and captured by strong capillary force through the grooves of the hexagonal channels (Fig. 1c-iii). The detailed methods for the fabrication of 3D MIN are provided in Supplementary Fig. 1. The geometrical elements of the hexagonal arrays were optimized to ensure robust adhesion by preventing crack initiation and propagation[23]. DNA-functionalized SWCNT (DNA/SWCNT) nanosensor dispersions were mixed with a polyacrylamide (PAAm) hydrogel (Fig. 1d) and embedded into microchannels. Here, PAAm was selected as a fluid capture matrix because of its water absorption capacity and the presence of abundant amide groups that form strong hydrogen bonds and electrostatically interact with SWCNTs[24], ensuring the functional integrity and performance of the nanosensors. We treated the 3D MIN with oxygen plasma for 3 min to stably integrate the DNA/SWCNT-containing pregel, enabling the nanosensor/hydrogel solution to disperse evenly and align uniformly within the microchannel geometry. Subsequently, the solution was poured onto a microchannel, excess material was removed, and the surface was thermally cured (Fig. 1e). The resulting 3D MIN was thin, flexible (area ~ 2×2 cm^2), and densely populated with hexagonally aligned 3D pillars and a nanosensor/hydrogel embedded in microchannel structures (Fig. 1f). The nIR image shows strong fluorescence from the patch, demonstrating stable integration of the nanosensor/hydrogel with the interface (inset, Fig. 1f). Scanning electron microscopy (SEM) images confirmed the structural uniformity of the patch (Fig. 1g). Each pattern unit has a channel width (w) of 200 μm, a channel height (h) of 300 μm, and a spacing (s) of 600 μm (Fig. 1g). We can design a 3D MIN multiarray for multivariate molecular tracing, for example, by integrating four different DNA/SWCNT nanosensors into a patch, each targeting various health indicators in human sweat (Fig. 1h). 3D MIN multiarrays can be effectively attached to rough and moist surfaces such as skin, enabling rapid biofluid collection. The confocal fluorescence microscopy image shows real-time capture of a target fluid into the microchannels through swelling of the nanosensor/hydrogel (inset, Fig. 1h).

Design and synthesis of the DNA/SWCNT nanosensor library

For 3D MIN applications, we targeted low-volume human sweat, which has a low secretion rate and contains more than one hundred analytes[25]. Moreover, developing a good adhesion interface to capture slow sweat secretion on dynamic skin surfaces is crucial for advanced healthcare. However, to date, in the field, only high-rate secretion of sweat over ~ 1.5 μL/min·cm^2 induced by exercise or iontophoresis has been detected, primarily targeting relatively easily detectable components[26]. We aimed to trace 15 challenging sweat analytes, vitamins, amino acids, and metabolites (Fig. 2a). For the multivariate tracing of these target analytes, we utilized the corona phase molecular recognition (CoPhMoRe) of DNA/SWCNTs, which modulates nIR fluorescence intensity (Fig. 2b)[27–33]. SWCNTs exhibit high mechanical stability, and DNA functionalization forms stable corona interfaces through phosphate interactions and π-π stacking[32,34], providing long-term stability and resistance to photobleaching under diverse biosurface conditions[27,35–37]. SWCNTs were suspended with $n = 20$ DNA sequences capable of forming corona phases at the SWCNT surface, producing structurally diverse corona phases to allow for the sampling of a range of free volumes and chemical interactions with sweat components (Supplementary Fig. 2a). Ultraviolet–visible-nIR (UV–vis-nIR) absorption spectroscopy revealed distinct absorption peaks in the synthesized DNA/SWCNT dispersions, specifically for the E_{11} and E_{22} transitions, demonstrating the successful isolation and suspension of individual SWCNTs (Supplementary Fig. 2b).

Next, dynamic light scattering (DLS) confirmed that the SWCNT sensors were dispersed uniformly at a consistent size (Supplementary Fig. 2c). The real-time responses of the resulting nIR fluorescence emissions from the nanosensor library were recorded, and the resulting 20×15 heatmap of molecular binding revealed distinct fluorescence responses $(I - I_0)/I_0$ (Fig. 2c). Here, I_0 and I represent the integrated nIR intensities of the nanosensors at $t = 0$ and after analyte injection, respectively. Each nanosensor showed a specific turn-on or turn-off response to its target analyte, with response intensity ranging from − 74% to 3500%. Based on the screening results, we selected four corona nanosensors for further characterization and as candidates for the multiarray system: $(AC)_{15}$/SWCNT for riboflavin (vitamin B2), $(AGCA)_7$/SWCNT for pyridoxine (vitamin B6), $(ACCA)_7$/SWCNT for folic acid (vitamin B9), and $(ACA)_{10}$/SWCNT for cortisol, ensuring that

https://doi.org/10.1038/s41467-025-58425-x

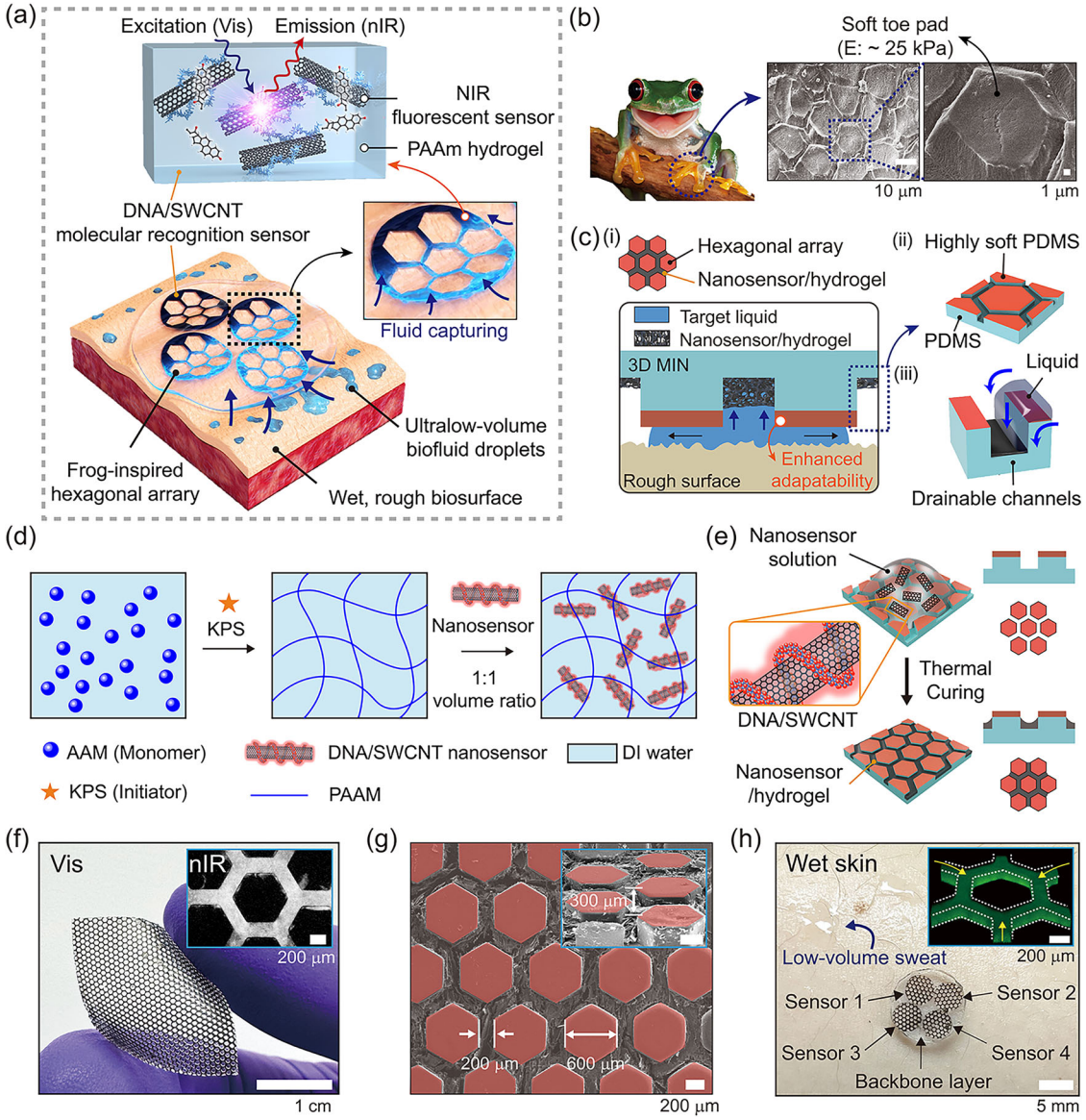

Fig. 1 | Bioinspired 3D microstructred patch integrated with optical nanosensors (3D MIN) for ultralow-volume fluid tracing. a Schematic illustration of the adhesion and molecular sensing mechanism of 3D MIN (3D microstructured patch integrated with optical nanosensors) on rough and wet human skin. (**b**) Hexagonal 3D microstructures observed in the toe pads of frogs (*Rhacophorus pardalis*). The hexagonal toe pads of frogs are covered with a soft layer with a modulus of approximately 25 kPa. Image in (**b**) adapted from © iStock.com (Asset ID: 1049028724), used under a Royalty-Free License. **c** Schematic illustrations of (i) 3D MIN on wet and rough surfaces, (ii) the highly soft polydimethylsiloxane (PDMS)-coated hexagonal array, and (iii) the drainage and biofluid-capturing effects facilitated by the hexagonal channel structure. **d** Schematic illustration of the synthetic process of the nanosensor/hydrogel and interactions involved in the network of the hydrogel. **e** Monolithic process for integrating the DNA/SWCNT (Single-Walled Carbon Nanotube) nanosensor into 3D MIN. **f** Photograph of the 3D MIN patch. Inset: Near-Infrared (nIR) image of 3D MIN. **g** Top-view scanning electron microscope (SEM) image of 3D MIN. Inset: Cross-sectional SEM image. **h** Photograph of a 3D MIN multiarray conformally attached onto a wet and rough human skin surface. Inset: A confocal image of a nanosensor/hydrogel within 3D MIN that is swollen due to liquid absorption.

each nanosensor exhibited the strongest response to its target analyte without overlap[27,32]. To evaluate sensor specificity, we tested a mixed analyte solution with three non-target analytes fixed at 1 μM while varying the target analyte concentration. Each nanosensor exhibited a fluorescence response proportional to the target analyte, with a response magnitude comparable to that observed for the single analyte, confirming specificity even in the presence of multiple analytes (Supplementary Fig. 3). These selected nanosensors not only demonstrated specificity but also targeted biologically significant molecules: vitamin B2, is an antioxidant involved in the prevention of many chronic diseases, vitamin B6 aids in neurotransmitter synthesis, vitamin B9 is crucial for preventing anemia and promoting early neurodevelopment, and cortisol is a key biomarker of stress response[38–40]. By simultaneously measuring vitamins B2, B6, and B9 and cortisol levels, we can uncover correlations between stress response and diseases related to specific vitamin deficiencies. Although we characterized the four nanosensors, CoPhMoRe nanosensors can be functionalized with diverse recognition elements, including polymers, proteins, and aptamers[41–43]. This versatility supports multiple sensor configurations in the 3D MIN, with each functionalized SWCNT operating independently. Consequently, additional sensors can be incorporated without altering the platform, enabling an unlimited combination of nanosensors for broader applications.

https://doi.org/10.1038/s41467-025-58425-x

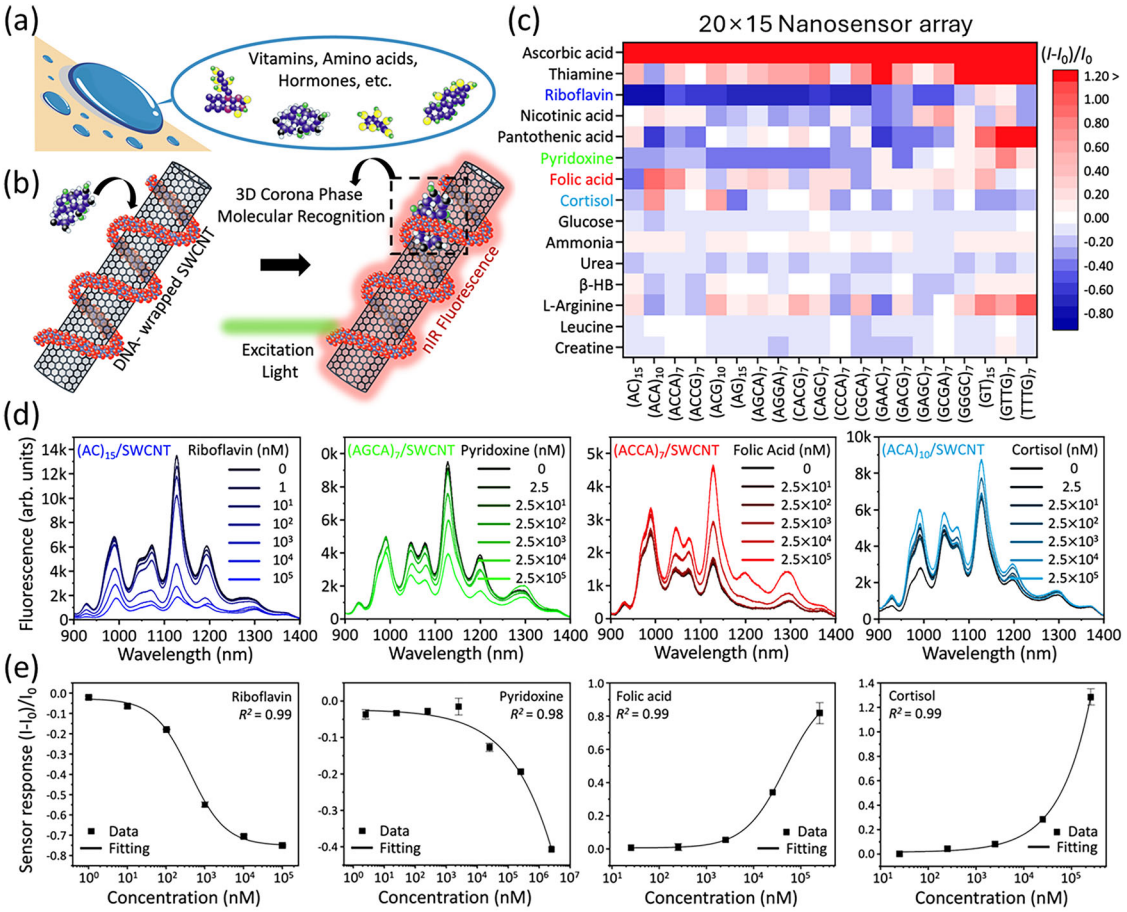

Fig. 2 | DNA/SWCNT nanosensor library for 3D MIN integration. Illustration of (**a**) target molecules in human sweat and (**b**) the molecular recognition mechanism of the DNA/SWCNT nanosensor. **c** High-throughput screening results of the DNA/SWCNT nanosensor array ($n = 20$) for target molecules ($n = 15$) in a low-volume of human sweat. **d**, **e** Calibration curve of the four nanosensors fitted with Hill's model. The error bars represent mean ± standard deviation ($n = 3$ independent samples).

The nIR responses of our sensor were recorded across a wide range of analytes at nanomolar to micromolar concentrations; this concentration range was selected because it matches the standard detection range for human sweat (Fig. 2d)[26,44,45]. Each selected nanosensor showed a dynamic increase or decrease in the nIR signal for each target analyte proportional to the analyte concentration. We plotted the calibration curve of the nanosensors and calculated the limit of detection (LOD) (Fig. 2e). Each sensor showed values of 1.74, 323, 991, and 2270 nM for vitamins B2, B6, and B9 and cortisol, respectively; these values were calculated by defining the nanosensor response in the buffer as a noise (σ) and using a signal corresponding to three times this noise level.

Drainage and fluid capture properties of 3D MIN

To demonstrate the fluid capture properties of 3D MIN, we prepared surfaces without a hydrogel (3D MIN w/o hydrogel) and with a hydrogel (3D MIN w/hydrogel). We investigated capillarity-driven liquid drainage via 3D MIN w/o hydrogel, which was influenced by the separation height (h) between the fluid and the substrate (Fig. 3a). When $h > h_1$ (Stage I), the liquid predominantly underwent radial squeeze-out[20–22,46,47]. As h approached h_1 (Stage II), the flow shifted toward the 3D channels, becoming the primary source of friction until $h < h_2$, where viscous resistance was encountered[20,22,46,47]. The drainage criterion based on fluid dynamics is expressed as[20,22]:

$$h(t) = \left(\frac{1}{h_0^2} + \frac{\alpha \cdot p \cdot t}{\mu D_0^2} \right)^{-\frac{1}{2}} \quad (1)$$

where $h(t)$ is the separation height, h_0 is the initial height of the liquid film (~534.5 mm), α is the order unity (~$4/3\pi$), p is the squeezing pressure, t is the time, μ is the viscosity of the water (~8.9×10^{-4} Pa•s), and D_0 is the lattice constant. Detailed numerical derivations for the model are shown in Supplementary Note 1 and Supplementary Table 1. The time and $h(t)$ model, plotted against experimental data, showed data alignment with fluid behavior during radial squeeze-out ($h > h_1$) and channel drainage ($h_1 > h > h_2$) (Fig. 3b). Fluorescence microscopy confirmed the fluid behavior at each stage (red and blue dots in Fig. 3b). The time to reach the drainage height (h_1) depends on the preload applied (Supplementary Fig. 4). Without an external preload, the patch's weight alone induced drainage. Applying a 2.0 N preload accelerated the process, reducing the time to 0.5 ms from 252 ms.

The 3D MIN w/hydrogel efficiently captured target biofluids by absorbing drained nanofluids, causing the hydrogel to swell and expand (Fig. 3c). Dried hydrogels in 3D microchannels can facilitate drainage by reducing the channel height and effectively capturing nanofluids through the hydrogel meniscus formed inside the channels (Supplementary Fig. 5). This liquid movement is driven by the surface energy gradient between the hydrophilic hydrogel and hydrophobic PDMS, where the drained nanofluid can be absorbed into the hydrogel through the meniscus (Supplementary Fig. 6)[18,48]. Fourier transform infrared (FTIR) analysis was used to investigate the chemical transitions occurring within the nanosensor/hydrogel during gel formation (Supplementary Fig. 7a). The embedded nanosensor/hydrogel forms stable bonds via hydrogen interactions (for detailed explanations, see Supplementary Note 2 and Supplementary Table 2). The stable

https://doi.org/10.1038/s41467-025-58425-x

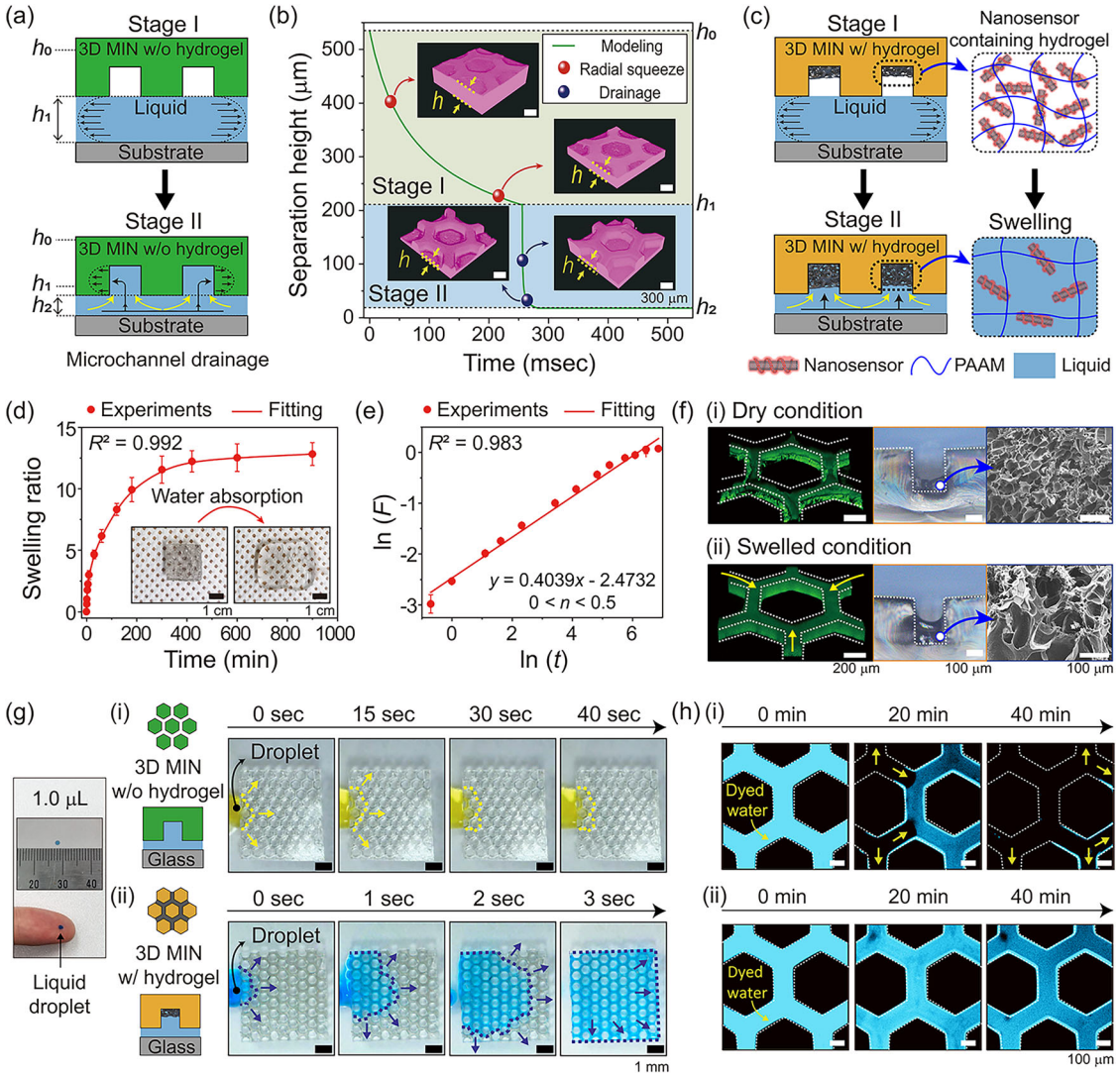

Fig. 3 | Drainage and nanofluid capture capability of 3D MIN. a Illustration of drainage in 3D MIN without hydrogel induced by the hexagonal channels and the characteristic fluid movement zones (Stages I and II). **b** Fluid drainage profile of 3D MIN without hydrogel with separation height and time. **c** Illustration of the liquid capture characteristics of 3D MIN with hydrogel. **d** Swelling ratio of the nanosensor-containing hydrogels (nanosensor/hydrogel) over time. Inset images of hydrogels swollen by water. **e** Swelling behavior of the nanosensor/hydrogel in DI water. **f** Confocal fluorescence microscopy images of Rhodamine B diluted in distilled water (left), optical microscopy images (center), and SEM images (right) of the hydrogel (i) before and (ii) after swelling. **g** Time series photographs of extremely low-volume fluid (1 μL) capture via (i) 3D MIN w/o hydrogel and (ii) w/hydrogel. The yellow and blue droplets were both dyed with water-soluble ink. Inset (left): photograph of a 1.0 μL liquid droplet on a ruler and fingertip. **h** Time series confocal microscopy images representing the fluid retention capability of (i) 3D MIN w/o hydrogel and (ii) w/hydrogel. The error bars in (**d**, **e**) represent mean ± standard deviation (n = 3 independent samples).

hydrogel network with DNA/SWCNT is formed by PAAm chain cross-linking through hydrogen bonding (Supplementary Fig. 7b)[49,50]. The swelling ratio of the nanosensor/hydrogel, as measured by immersion in distilled water, reached an equilibrium ratio of ~12.8 g/g (Fig. 3d). The swollen nanosensor/hydrogel is shown in the inset of Fig. 3d. This swelling mechanism of the hydrogel can be described based on the Fickian diffusion model[51,52] (see Supplementary Note 3 for a detailed derivation). From the Fickian diffusion model, we confirmed that n is less than 0.5 (Fig. 3e). This finding indicated that Fickian diffusion was dominant, with solvent molecules penetrating the internal spaces of the hydrogel to absorb the liquid[52]. We used confocal fluorescence microscopy, optical microscopy, and SEM to monitor hydrogel swelling within microchannels before (Fig. 3f-i) and after (Fig. 3f-ii) water absorption. The embedded dried hydrogel within the 3D MIN absorbed the target liquid, leading to volume expansion. The cross-sectional SEM images of the freeze-dried hydrogel revealed a microporous structure, with the pore size increasing upon swelling. We observed the instantaneous capture of 1.0 μL of dyed water in 3D MIN w/hydrogel on a glass surface (Fig. 3g). The 3D MIN w/o hydrogel did not capture yellow-dyed water even after 40 s, whereas the 3D MIN w/hydrogel captured blue-dyed water within 3 s. The real-time videos of these processes are shown in Supplementary Movie 1 and 2. Moreover, the 3D MIN w/hydrogel efficiently retained the absorbed fluid (Fig. 3h). Using confocal microscopy, we observed that the liquid in 3D MIN w/o hydrogel evaporated within 40 min (Fig. 3h-i) due to edge evaporation, whereas the 3D MIN w/hydrogel showed minimal evaporation, retaining the liquid significantly longer (Fig. 3h-ii).

Adhesion properties of 3D MIN

We measured the adhesion strengths of 3D MIN on surfaces with roughness (R_a) values of 80 μm and 160 μm, which were prepared via soft polyurethane acrylate (s-PUA). The cross-sectional SEM images of the prepared surfaces are shown in Supplementary Fig. 8. Higher R_a values indicate rougher surfaces. We compared the

https://doi.org/10.1038/s41467-025-58425-x

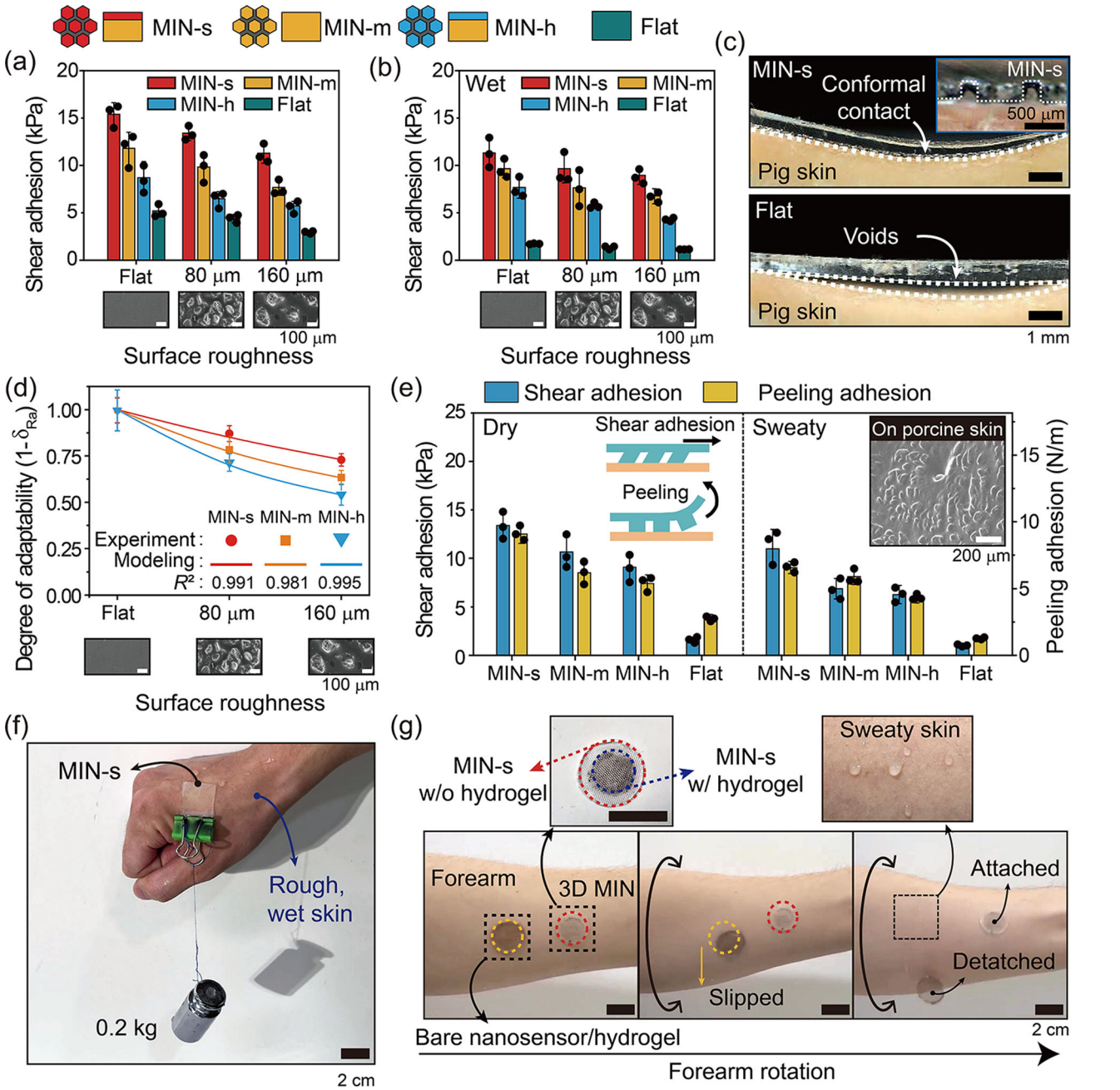

Fig. 4 | Adhesion performance of 3D MIN on wet and rough surfaces. Adhesion performance of 3D MIN with a soft hexagonal pad (3D MIN-s), medium hexagonal pad (3D MIN-m), hard hexagonal pad (3D MIN-h), and flat patches on (**a**) dry and (**b**) wet surfaces with varying roughnesses values (R_a = 0, 80, and 160 μm). **c** Cross-sectional optical microscopy images of MIN-s and flat patches in contact with porcine skin. **d** Degree of adaptability profiles for MIN-s, MIN-m, and MIN-h (R_a = 0, 80, and 160 mm). **e** Shear and peeling resistance of MIN-s, MIN-m, MIN-h, and flat patches on porcine skin under dry and sweaty conditions. Inset: SEM images of target porcine skin. **f** Photograph of MIN-s attached to rough and wet human skin with weights (0.2 kg) suspended in the shear direction. **g** Photograph of 3D MIN and a bare nanosensor/hydrogel layer without any microstructure on wet skin with the forearm rotating. The error bars in (**a**, **b**, **d**, **e**) represent mean ± standard deviation (n = 3 independent samples).

adhesion performance of four samples: 3D MIN with a soft hexagonal pad (MIN-s), a medium hexagonal pad (MIN-m), a hard hexagonal pad (MIN-h), and a flat sample (Flat). Hexagonal pads were transferred onto the surfaces of s-PDMS, 20:1 PDMS, and 10:1 PDMS with different elastic moduli (Supplementary Fig. 9). MIN-s had the greatest adhesion strength on dry surfaces: 15.4 kPa on flat surfaces, 13.4 kPa on surfaces with R_a values of 80 μm, and 11.2 kPa on surfaces with R_a values of 160 μm (Fig. 4a). On wet surfaces, the adhesion strengths were 11.3 kPa on flat surfaces, 9.6 kPa on surfaces with R_a values of 80 μm, and 6.7 kPa on surfaces with R_a values of 160 μm, all in the shear direction (Fig. 4b). The s-PDMS layer enhanced asperity conformity, improving adhesion on rough substrates. MIN-s showed conformal contact with rough porcine skin, unlike the flat sample, which had voids indicating poor contact (Fig. 4c).

On this basis, we developed an adhesion model for MIN-s, considering total capillary-based attachment (σ_c) resulting from capillary bridge formation and contact interface adhesion in wet environments. Under wet conditions, capillary forces dominate over viscous forces[21]. For MIN-s under wet conditions, σ_c is

expressed as[53,54]:

$$\sigma_c = n_{area} \cdot \frac{\sqrt{3}}{2} \cdot (SR_H \cdot w^2) \cdot \gamma \cdot \left(\frac{\cos\vartheta_1 + \cos\vartheta_2}{h}\right) + n_{area} \cdot 2\sqrt{3} \cdot SR_H \cdot w \cdot \gamma \quad (2)$$

where n_{area} is the number of patterns per unit area (~180/cm^2), SR_H is the space ratio of the hexagonal microchannel, w is the width of the microchannel, γ is the surface tension of water, θ_1 and θ_2 are the contact angles of DI water on the patch and the substrate, respectively, and h is the separation height (see Supplementary Note 4 for a detailed derivation). Separation occurs on rough surfaces due to interfacial interactions between the adhesive patch and the surface. The separation height (δ_{R_a}) increases with weaker interactions and decreases with stronger interactions. This correlation can be interpreted on the basis of the adhesive stress for each hexagonal pad relative to surface roughness, which showed an approximately linear relationship based on experimental data (see Supplementary Fig. 10 and Supplementary Note 5)[55,56]. Hence, the degree of adaptability of the soft hexagonal pad on a rough surface ($1 - \delta_{R_a}$) can be expressed as: $1 - \delta_{R_a} \approx 1/(\alpha R_a + 1)$. Here, R_a is the average roughness, δ_{R_a} is the compensation factor on a rough substrate with R_a, and α is the conformity parameter. MIN-s showed greater adaptability (~73%) to wet rough surfaces (R_a = 160 μm) than MIN-m (~65%) and MIN-h (~56%) (Fig. 4d). Consequently, MIN-s had a lower adhesion reduction rate on rough surfaces because the soft-coated layer showed improved adhesion and conformity to surface irregularities. The van der Waals-based adhesion mechanism under dry conditions is summarized in Supplementary Note 6.

We subsequently conducted adhesion tests on porcine skin with different orientations (Fig. 4e). MIN-s exhibited the highest adhesive strength under both dry (~13.3 kPa) and sweaty (~11.3 kPa) conditions, followed by MIN-m, MIN-h, and on flat surfaces. Furthermore, MIN-s displayed the highest resistance to peeling under dry (~8.7 N/m) and sweaty (~6.6 N/m) conditions because its surface softness enhanced interface interactions, and more energy was required for separation[57]. We affixed the MIN-s patch to a human hand and applied a 0.2 kg shear force under wet conditions. The patch remained attached to the human hand, highlighting its strong adhesion (Fig. 4f). Furthermore, owing to the biocompatibility of 3D adhesive structures and nanosensors/hydrogels[58,59], minimal skin irritation was observed when 3D MIN was applied for 6 h, with or without hydrogels, unlike conventional chemical adhesives (Supplementary Fig. 11). On a sweaty forearm, we tested a 3D MIN (both MIN-s w/o hydrogel and MIN-s w/ hydrogel) and a nanosensor/hydrogel without a 3D microstructure (Fig. 4g). The bare nanosensor/hydrogel detached after dynamic up-and-down movements due to water absorption and swelling, whereas the 3D MIN maintained stable adhesion even after eight dynamic rotations.

In vitro and on-body characterization of 3D MIN

For ultralow-volume fluid tracing, we used an in vitro sweating skin model to evaluate the performance of 3D MIN. A syringe pump connected with artificial skin released fluid at a controlled fluid rate to the 3D MIN (Supplementary Fig. 12). The nIR fluorescence response was monitored in real time via an nIR microscope. To clearly visualize the microfluidics within the 3D MIN, we first employed the vitamin C sensor, $(ACG)_{10}$/SWCNT, which exhibited the strongest turn-on signal in our library. Figure 5a shows the real-time spatial responses from 3D MIN to varying concentrations of vitamin C. The 3D MIN exhibited continuous turn-on responses: −22.1% at 0 μM, 135% at 10 μM, 266% at 40 μM, 532% at 100 μM, and 932% at 200 μM vitamin C (Fig. 5a). The 3D MIN showed a slight response to DI water, attributed to hydrogel swelling, which slightly alters the SWCNT nanosensor distribution and decreases the average signal per unit (Supplementary Fig. 13). We compared the calibration curves of the 3D MIN and the liquid phase (Supplementary Fig. 14). While the detectable concentration ranges were similar, the LOD in the 3D MIN was approximately one order higher, which might be due to the nanosensor's embedding within the hydrogel matrix, limiting analyte interactions and attenuating nIR signals compared to aqueous solutions. For flow rate experiments, we used a 1 mM vitamin C solution and measured the spatial sensor response of 3D MIN at flow rates of 0.5, 0.25, and 0.1 μL/min•cm^2 to simulate daily sweat secretion (0.37 μL/min•cm^2). The response times (T_{90}) were calculated to be 28.3 s at 0.5 μL/min•cm^2, 40.0 s at 0.25 μL/min•cm^2, and 45.6 s at 0.1 μL/min•cm^2 (left, Fig. 5b). Based on this database if sweat rate measurement could also be integrated during the actual application, the device would serve as a more precise platform for quantifying analytes. Fluid capturing occurred efficiently even at a flow rate of 0.1 μL/min•cm^2, with a gradual increase in nIR emission (right, Fig. 5b). The nIR emission video at a flow rate of 0.1 μL/min•cm^2 is provided in Supplementary Movie 3. Notably, while existing wearable sweat sensors require a minimum sampling time of 100 s to 20 min and an average sampling volume of 1 μL, our 3D MIN can detect 75 nL of fluid in 45 s at a rate of 0.1 μL/min·cm^2 (Fig. 5c)[16,17,60–68]. The detailed numerical values of the references in Fig. 5c are shown in Supplementary Table 3.

In addition, among the selected four nanosensors, the 3D MIN targeting cortisol was further evaluated, showing turn-on responses of 2.9, 3.6, 67.8, and 117.5% for 1 μM, 10 μM, 100 μM, and 1 mM cortisol, respectively. Saturation time was determined to be 68 s at a flow rate of 0.1 μL/min·cm^2 (Supplementary Figs. 15 and 16). These results demonstrate the potential application of the 3D MIN nanosensor for on-body stress monitoring. To demonstrate the multivariate tracing abilities of our system, we fabricated a 3D MIN multiarray using the four selected nanosensors (Fig. 2d) and measured spatiotemporal nIR responses via a stand-off nIR camera (Fig. 5d and Supplementary Fig. 17). The experiment was conducted using 1 mM solutions of vitamins B2, B6, B9, and cortisol. nIR images of the 3D MIN multiarray show distinct molecular fingerprints to different biofluids (Fig. 5e), with responses ranging from −40.4% to +32.6% (Supplementary Fig. 18). While we demonstrated the capabilities of four arrays, a multiarray configuration can be achieved with more 3D MIN units by adjusting the backbone layer size and unit shape.

To demonstrate low-volume fluid capture on rough and dynamic surfaces, we attached a 3D MIN multiarray, embedding one slot with a vitamin C sensor and the other slots empty onto a human forehead and measured the analytes (e.g., vitamin C) present in sweat in real-time. The human forehead was selected for this test because it undergoes substantial mechanical deformation and dynamic movements with different facial expressions[69]. Before on-body measurements, we confirmed that the 3D MIN integrated with the $(ACG)_{10}$/SWCNT nanosensor responded predominantly to vitamin C in artificial sweat containing 15 different analytes at a concentration of 10 μM each, excluding vitamin C. Although the composition of this artificial sweat differs from actual human sweat, it includes analytes with molecular weights and moieties similar to the target to address potential interference. This ensures the approach's relevance for evaluating the selectivity and sensitivity of the sensor in mixed solutions (Supplementary Fig. 19). Three human subjects who attached the 3D MIN multiarray ingested different doses of vitamin C (0 g, 1.5 g, and 3 g), and sweat samples were collected without any exercise or iontophoresis, instead sweat was collected during sedentary and daily activities, in which sweat secretion is typically minimal (Fig. 5f). First, to confirm the presence of vitamin C in human sweat, high-performance liquid chromatography (HPLC) analysis was performed. Sweat samples collected at 0 min and 150 min post-ingestion showed a vitamin C peak matching that of a pure vitamin C solution, with peak intensity increasing proportionally over time, confirming the presence of vitamin C in captured sweat samples (Supplementary Fig. 20). nIR images

https://doi.org/10.1038/s41467-025-58425-x

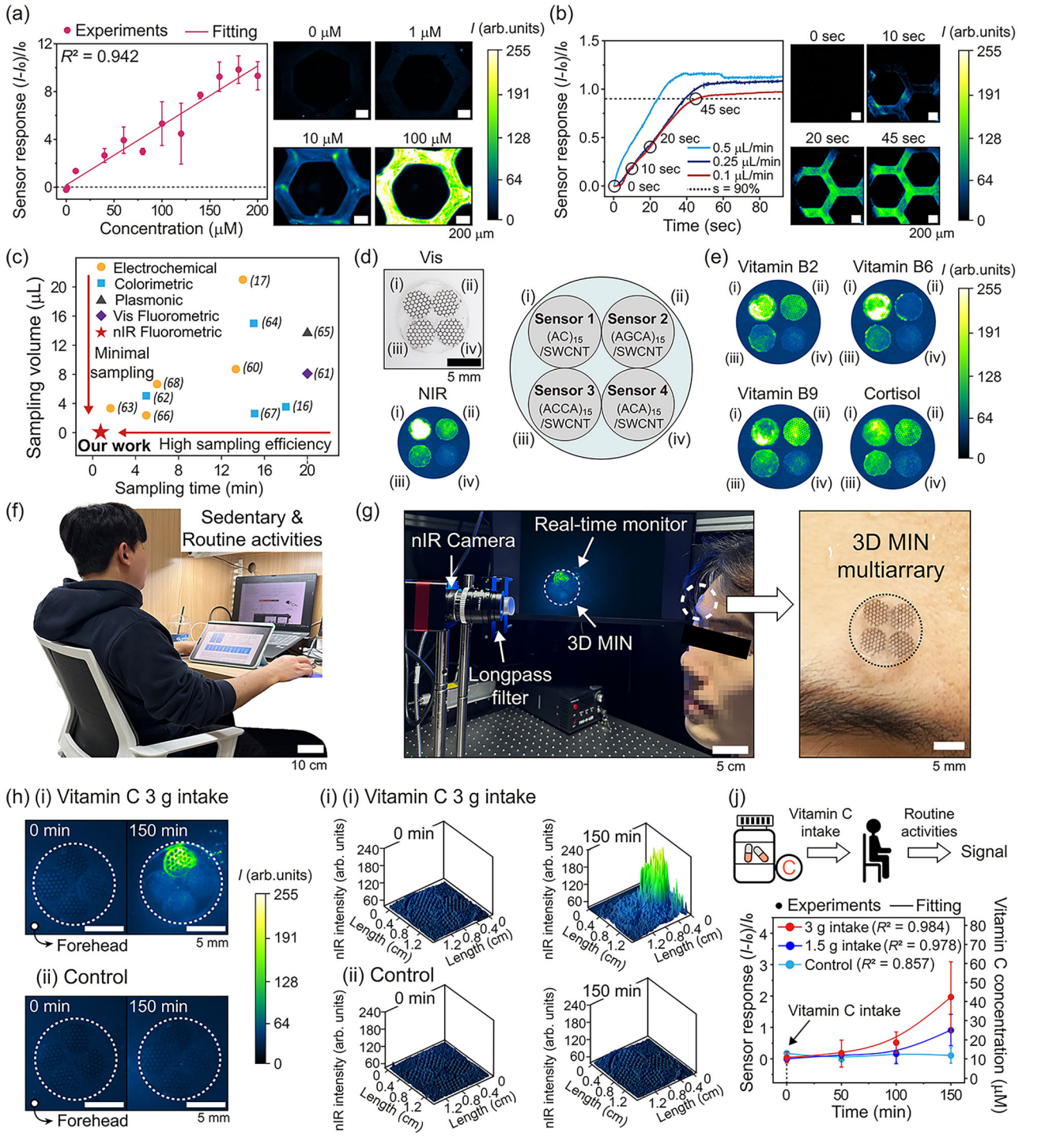

Fig. 5 | Spatiotemporal molecular tracing of low-volume fluid via 3D MIN. **a** Spatial sensor responses of 3D MIN to ascorbic acid (vitamin C) under a wide range of concentrations. The signal is calculated by the average nIR intensity variation from a single unit of 3D MIN, and the data represent the mean value of $n = 3$ replicates. **b** Real-time response of 3D MIN to vitamin C at various flow rates (0.1, 0.25, and 0.5 μL/min·cm^2). **c** Comparison of the sampling times and volumes reported in previous research on sweat tracing. **d** Photograph (top-left), nIR image (bottom-left), and schematics of the 3D MIN multiarray. **e** Molecular fingerprint capabilities of the 3D MIN multiarray for vitamins B2, B6, and B9 and cortisol. **f** Photograph of a study participant with the 3D MIN multiarray attached while performing routine daily activities. **g** Stand-off nIR camera setup for remote imaging of 3D MIN (left). A 3D MIN array attached to a study participant with only one slot embedded with vitamin C sensor was used to highlight the spatial mapping capability of the 3D MIN attached to the subject in situ (right). **h** Real-time nIR images of the 3D MIN on foreheads (i) before and 150 min after vitamin C (3 g) intake and (ii) the control group (ii). **i** 3D spatial nIR response map from 3D MIN multiarray responses for (i) the vitamin C (3 g) intake group and (ii) the control group. **j** nIR sensor responses (left y-axis) and the estimated concentration of vitamin C (right y-axis) from three independent subjects ($n = 3$) measured using 3D MIN at 0, 50, 100, and 150 min following the intake of 0, 1.5, or 3 g of vitamin C. The error bars in (**a**, **j**) represent mean ± standard deviation ($n = 3$ independent samples). In panel (**j**), the healthcare and medical icon was created by Phoebeicons – Flaticon (https://www.flaticon.com/free-icons/healthcare-and-medical), and the seat icon was created by Freepik – Flaticon (https://www.flaticon.com/free-icons/seat).

were measured at 0 min, 50 min, 100 min, and 150 min after Vitamin C ingestion, and signals were monitored via a stand-off nIR camera (Fig. 5g). Considering the hydrogel's swelling ratio (~ 12.8 g/g), it can sufficiently accommodate the small amount of sweat secreted during sedentary and routine activities without compromising sensor performance[70,71]. Furthermore, we employed the 3D MIN as a single-use patch and monitored the nIR signals at each time point to avoid prolonged excessive fluid absorption, thereby preserving the sensor's rapid response. nIR images of the 3D MIN multiarray attached to the subject who ingested 3 g of vitamin C (Fig. 5h-i and Supplementary Movie 4) clearly revealed spatially distinct nIR responses at 0 min and 150 min compared to control dose (0 g) (Fig. 5h-ii). Compared to the control group (Fig. 5i-ii), different localized regions in the vitamin C group exhibited distinct nIR response pixels within a diameter of 1 cm, providing high spatiotemporal resolution (Fig. 5i-i). Sensor responses increased over time with the highest response observed when the group ingested 3 g of vitamin C, followed by 1.5 g, while negligible response was observed during the control experiment with no vitamin C intake (Fig. 5j). By using first-order binding model (Supplementary Note 7), we estimated the concentration of vitamin C in captured sweat based on the measured nIR responses, which ranged from 5 μM to 60 μM and aligned with previously reported vitamin C concentration ranges typically found in sweat[26]. With sweat-blood correlation coefficients[72], the 3D MIN sensor enables the estimation of blood vitamin C levels through sweat vitamin C measurements, providing a non-invasive alternative. Thus, this technique allows for the real-time visualization of the sweat secretion, even at extremely low-volumes and rates of secretion. This represents a significant advantage over conventional electrical or electrochemical sweat sensing methods. Overall, the ability of 3D MIN to detect low-volume fluids at low secretion rates on dynamic and rough on-body surfaces was validated.

In this study, we monolithically integrated optical nanosensors with a 3D microstructured interface for real-time, spatiotemporal molecular tracing of extremely low-volume fluids. Inspired by tree frog toe pads, we designed this form factor with hexagonally aligned 3D pillars coated with s-PDMS and microchannels, which enabled the simultaneous and efficient capture and sensing of biofluids within 0.25 ms without preloading and with strong adhesion even on wet biosurfaces. With conformal contact with rough surfaces, 3D MIN achieved high adaptability of up to 73% and stable adhesion with shear strengths of 15.4 kPa and 11.3 kPa on dry and wet rough substrates, respectively. For tracing applications, we synthesized a 20 × 15 array of DNA/SWCNT nanosensors with molecular recognition capabilities and selected four specific nanosensors to trace key biomarkers in low-volumes of human sweat (vitamins B2, B6, B9, and cortisol). 3D MIN enabled the rapid detection of 75 nL of sweat within 45 s at a flow rate of 0.1 μL/min·cm². We demonstrated the potential of the multiarray configuration to simultaneously detect these indicators, providing distinct molecular fingerprints. We demonstrated the effective on-body use of 3D MIN on the forehead to capture and analyze human sweat in real-time without the need for exercise or iontophoresis. All nIR emissions from the optical nanosensors were measured via a stand-off camera, enabling in situ, real-time, and high spatiotemporal resolution sensing within 1 cm without additional accessories. This sensor form factor provides opportunities to maximize the sensing characteristics of SWCNT nanosensors and a wide range of other optical probes.

Methods

Fabrication of 3D MIN

To fabricate the frog-inspired hexagonal pattern master, a silicon mold with negative hexagonal patterns (width = 200 μm, height = 300 μm, spacing = 600 μm) was prepared via photolithography and reactive ion etching. The mold was treated with a fluorinated self-assembled monolayer solution of (tridecafluoro-1,1,2,2-tetrahydrooctyl)-trichlorosilane (FOTCS; Gelest Corporation, USA) diluted to 0.03 M with anhydrous heptane (Samchun Chemical, South Korea) under argon. Positive hexagonal patterns were obtained by replica molding each mold with 20:1 PDMS (Sylgard 184, Dow Corning, USA) for 2 hr at 60 °C. A soft hexagonal pad on 3D MIN (3D MIN-s) was formed by spin-coating s-PDMS (PDMS + polyethyleneimine, 40 μL/10 g PDMS) on a silicone substrate at 800 rpm for 1 min. A hexagonal patch was selectively transferred by inking the s-PDMS layer on a silicon wafer for 5 s without pressure, then cured at 90 °C for 1 h on glass. Similarly, 20:1 and 10:1 PDMS were applied to 3D MIN with medium and hard hexagonal pads (3D MIN-m, 3D MIN-h), respectively (Supplementary Fig. 1a). PAAm hydrogel was prepared by mixing acrylamide (AAm), potassium persulfate (KPS), and water. To prepare it, 5 g AAm, 0.05 g KPS, and 10 mL DI water were vortexed for 5 min. The DNA/SWCNT nanosensor solution was then mixed with pregel PAAm hydrogel (1:1 volume) vortexed again for homogeneity (Fig. 1d). 3D MIN was treated with oxygen plasma for 3 min to achieve stable integration with the pregel (Supplementary Fig. 1b). The patch was placed on a Teflon-coated substrate, and 250 mL/cm² of DNA/SWCNT–hydrogel mixture was poured on top to fill microchannels. The excess composite solution was wiped off, leaving the solution to fill hexagonal channels, forming a concave meniscus via surface tension. The sample was cured at 80 °C for 20 min.

nIR imaging of 3D MIN

Quantitative in vitro testing of the microfluidic performance of the patch was performed by a simple, artificial sweat pore system in the nIR microscopy setup (Supplementary Fig. 12). To mimic a human sweat gland, a 0.5 mm inner diameter silicone pipe was connected to a syringe pump (NE-1000, New Era Pump Systems) and a PDMS cast. The syringe pump controlled the flow rate of the fluid from 0.1 μL/min to 1.5 μL/min. Porcine skin was punctured to create a hole such that the pipe was located inside the porcine skin, and as a result, water was discharged from the syringe to the porcine skin via the pipe. Then, 3D MIN was attached to the porcine skin. The multiarray experiment was conducted using an nIR camera (NINOX OWL 640 T Digital VIS-SWIR Camera) equipped with a 900 nm longpass filter to detect nIR spectral light response. The multiarray was designed to hold four spatially encoded 3D MIN arrays. All four nanosensors were fabricated via the 3D MIN fabrication method, including each of the sensors. The resulting 3D MIN arrays were then punched into circular sensor shapes with diameters of 4.5 mm via a punch device. These circular sensors were attached to round backbones with diameters of 1 cm, with a thin PDMS coating on the backside, and cured together. The multiarray was placed on a non-reflective black backstage, and nIR images were collected by installing the nIR camera at a distance of 20 cm in the vertical direction. From the side, the multiarray was excited via a collimator and diffuser lens combined with a 721 nm laser, and no external light was present in the darkroom (Supplementary Fig. 16). The multiarray was placed on a non-reflective black background, and only the excitation laser light was present in the darkroom to stimulate the SWCNT sensor. The excited SWCNTs emitted nIR PL, which was collected through the longpass filter integrated into the nIR camera. The image acquisition and processing of both the nIR microscopy and camera were performed using XCAP software (version 3.8) and Image J (version 1.54 f).

On-body sweat tracing

3D MIN patch experiments involving human subjects were performed after approval was initially received from the Institutional Review Board (IRB) for both subject and parental assent (IRB approval no. SKKU 2023-12-057), following school board policies. The sweat tracing experiments were conducted indoors on a day with an average temperature of 25 °C and 60% relative humidity. The subjects in the experimental group were not induced to sweat by any means, and

sweat detection was performed using naturally occurring sweat in the resting state. All nIR responses were measured via an nIR microscope and an nIR camera in a darkroom. The nIR microscope setup was identical to that shown in Supplementary Fig. 12 without the syringe pump system, and the nIR camera setup is shown in Fig. 5g. HPLC analysis (Agilent 1260/6130) was performed on a control sample (3 mL, 500 μM vitamin C solution) and sweat samples ($n = 5$) collected from two subjects during exercise using microtubes. 200 μL of sweat samples were collected from both subjects before and 150 min after consuming 3 g of vitamin C. All participants provided written informed consent for the publication of their images.

Reporting summary

Further information on research design is available in the Nature Portfolio Reporting Summary linked to this article.

Data availability

All the main data supporting the results of this study are available within the paper, Supplementary Information and Source data. Supplementary Information and Source data for all figures are provided in this paper. All raw and analyzed datasets generated during the study are available from the corresponding author upon request. Source data are provided in this paper.

References

1. Agrawal, K. V., Shimizu, S., Drahushuk, L. W., Kilcoyne, D. & Strano, M. S. Observation of extreme phase transition temperatures of water confined inside isolated carbon nanotubes. *Nat. Nanotechnol.* **12**, 267–273 (2016).
2. Galassi, T. V. et al. An optical nanoreporter of endolysosomal lipid accumulation reveals enduring effects of diet on hepatic macrophages in vivo. *Sci. Transl. Med.* **10**, eaar2680 (2018).
3. Neubert, E. et al. Chromatin swelling drives neutrophil extracellular trap release. *Nat. Commun.* **9**, 3767 (2018).
4. Zhou, F. et al. Tracing haematopoietic stem cell formation at single-cell resolution. *Nature* **533**, 487–492 (2016).
5. Rivera, V. M. et al. Regulation of protein secretion through controlled aggregation in the endoplasmic reticulum. *Science* **287**, 826–830 (2000).
6. Bernard, V., Young, J., Chanson, P. & Binart, N. New insights in prolactin: pathological implications. *Nat. Rev. Endocrinol.* **11**, 265–275 (2015).
7. Freedman, K. J. et al. Nanopore sensing at ultra-low concentrations using single-molecule dielectrophoretic trapping. *Nat. Commun.* **7**, 10217 (2016).
8. Tang, L. et al. Combined quantum tunnelling and dielectrophoretic trapping for molecular analysis at ultra-low analyte concentrations. *Nat. Commun.* **12**, 913 (2021).
9. Steinhauser, M. L. et al. Multi-isotope imaging mass spectrometry quantifies stem cell division and metabolism. *Nature* **481**, 516–519 (2012).
10. Regnier, F. E. High-performance liquid chromatography of biopolymers. *Science* **222**, 245–252 (1983).
11. Alseekh, S. et al. Mass spectrometry-based metabolomics: a guide for annotation, quantification and best reporting practices. *Nat. Methods* **18**, 747–756 (2021).
12. Heller, D. A. et al. Optical detection of DNA conformational polymorphism on single-walled carbon nanotubes. *Science* **311**, 508–511 (2006).
13. Kalkal, A., Kadian, S., Pradhan, R., Manik, G. & Packirisamy, G. Recent advances in graphene quantum dot-based optical and electrochemical (bio)analytical sensors. *Mater. Adv.* **2**, 5513–5541 (2021).
14. Mann, F. A., Galonska, P., Herrmann, N. & Kruss, S. Quantum defects as versatile anchors for carbon nanotube functionalization. *Nat. Protoc.* **17**, 727–747 (2022).
15. Kim, M. et al. Nanosensor-based monitoring of autophagy-assoc iated lysosomal acidification in vivo. *Nat. Chem. Biol.* **19**, 1448–1457 (2023).
16. Koh, A. et al. A soft, wearable microfluidic device for the capture, storage, and colorimetric sensing of sweat. *Sci. Transl. Med.* **8**, 366ra165 (2016).
17. Tu, J. et al. A wireless patch for the monitoring of C-reactive protein in sweat. *Nat. Biomed. Eng.* **7**, 1293–1306 (2023).
18. Baik, S. et al. Diving beetle-like miniaturized plungers with reversible, rapid biofluid capturing for machine learning-based care of skin disease. *Sci. Adv.* **7**, eabf5695 (2021).
19. Sempionatto, J. R. et al. An epidermal patch for the simultaneous monitoring of haemodynamic and metabolic biomarkers. *Nat. Biomed. Eng.* **5**, 737–748 (2021).
20. Banik, A. & Tan, K. T. Dynamic friction performance of hierarchical biomimetic surface pattern inspired by frog toe-pad. *Adv. Mater. Interfaces* **7**, 2000987 (2020).
21. Langowski, J. K. A., Dodou, D., Kamperman, M. & van Leeuwen, J. L. Tree frog attachment: mechanisms, challenges, and perspectives. *Front. Zool.* **15**, 32 (2018).
22. Persson, B. N. J. Wet adhesion with application to tree frog adhesive toe pads and tires. *J. Phys. Condens. Matter* **19**, 376110 (2007).
23. Kim, D. W. et al. Highly permeable skin patch with conductive hierarchical architectures inspired by amphibians and octopi for omnidirectionally enhanced wet adhesion. *Adv. Funct. Mater.* **29**, 1807614 (2019).
24. Dubey, R., Dutta, D., Sarkar, A. & Chattopadhyay, P. Functionalized carbon nanotubes: synthesis, properties and applications in water purification, drug delivery, and material and biomedical sciences. *Nanoscale Adv.* **3**, 5722–5744 (2021).
25. Baker, L. B. Physiology of sweat gland function: the roles of sweating and sweat composition in human health. *Temperature* **6**, 211–259 (2019).
26. Bariya, M., Nyein, H. Y. Y. & Javey, A. Wearable sweat sensors. *Nat. Electron.* **1**, 160–171 (2018).
27. Zhang, J. et al. Molecular recognition using corona phase complexes made of synthetic polymers adsorbed on carbon nanotubes. *Nat. Nanotechnol.* **8**, 959–968 (2013).
28. Bisker, G. et al. Protein-targeted corona phase molecular recognition. *Nat. Commun.* **7**, 10241 (2016).
29. Bakh, N. A. et al. Transcutaneous measurement of essential vitamins using near-infrared fluorescent single-walled carbon nanotube sensors. *Small* **17**, e2100540 (2021).
30. Mu, B. et al. Recent advances in molecular recognition based on nanoengineered platforms. *Acc. Chem. Res.* **47**, 979–988 (2014).
31. Nißler, R. et al. Remote near infrared identification of pathogens with multiplexed nanosensors. *Nat. Commun.* **11**, 5995 (2020).
32. Sultana, N., Dewey, H. M., Arellano, A. G. & Budhathoki-Uprety, J. Understanding the molecular assemblies of single walled carbon nanotubes and tailoring their photoluminescence for the next-generation optical nanosensors. *Chem. Mater.* **36**, 4034–4053 (2024).
33. Kruss, S. et al. Carbon nanotubes as optical biomedical sensors. *Adv. Drug Deliv. Rev.* **65**, 1933–1950 (2013).
34. Baughman, R. H., Zakhidov, A. A. & De Heer, W. A. Carbon nanotubes–the route toward applications. *Science* **297**, 787–792 (2002).
35. Boghossian, A. A. et al. Near-infrared fluorescent sensors based on single-walled carbon nanotubes for life sciences applications. *ChemSusChem* **4**, 848–863 (2011).

36. Kozawa, D. et al. A fiber optic interface coupled to nanosensors: applications to protein aggregation and organic molecule quantification. *ACS nano* **14**, 10141–10152 (2020).
37. Cho, S.-Y. et al. Cellular lensing and near infrared fluorescent nanosensor arrays to enable chemical efflux cytometry. *Nat. Commun.* **12**, 3079 (2021).
38. Ashoori, M. & Saedisomeolia, A. Riboflavin (vitamin B2) and oxidative stress: a review. *Br. J. Nutr.* **111**, 1985–1991 (2014).
39. Calderón-Ospina, C. A. & Nava-Mesa, M. O. B Vitamins in the nervous system: current knowledge of the biochemical modes of action and synergies of thiamine, pyridoxine, and cobalamin. *CNS Neurosci. Ther.* **26**, 5–13 (2020).
40. Shulpekova, Y. et al. The concept of folic acid in health and disease. *Molecules* **26**, 3731 (2021).
41. Hendler-Neumark, A. & Bisker, G. Fluorescent single-walled carbon nanotubes for protein detection. *Sensors* **19**, 5403 (2019).
42. Bisker, G. et al. Insulin detection using a corona phase molecular recognition site on single-walled carbon nanotubes. *ACS Sens.* **3**, 367–377 (2018).
43. Salem, D. P. et al. Chirality dependent corona phase molecular recognition of DNA-wrapped carbon nanotubes. *Carbon* **97**, 147–153 (2016).
44. Tang, Y.-M. et al. Relationships between micronutrient losses in sweat and blood pressure among heat-exposed steelworkers. *Ind. Health* **54**, 215–223 (2016).
45. Min, J. et al. Skin-interfaced wearable sweat sensors for precision medicine. *Chem. Rev.* **123**, 5049–5138 (2023).
46. Gupta, R. & Fréchette, J. Measurement and scaling of hydrodynamic interactions in the presence of draining channels. *Langmuir* **28**, 14703–14712 (2012).
47. Dhong, C. & Fréchette, J. Coupled effects of applied load and surface structure on the viscous forces during peeling. *Soft Matter* **11**, 1901–1910 (2015).
48. Zheng, Y. et al. Directional water collection on wetted spider silk. *Nature* **463**, 640–643 (2010).
49. Bai, L. et al. Comparison of hydrophilicity and mechanical properties of nanocomposite membranes with cellulose nanocrystals and carbon nanotubes. *Environ. Sci. Technol.* **51**, 253–262 (2017).
50. Sun, H. et al. Highly stretchable, transparent, and bio-friendly strain sensor based on self-recovery ionic-covalent hydrogels for human motion monitoring. *Macromol. Mater. Eng.* **304**, 1900227 (2019).
51. Wang, W. & Wang, A. Synthesis and swelling properties of pH-sensitive semi-IPN superabsorbent hydrogels based on sodium alginate-g-poly(sodium acrylate) and polyvinylpyrrolidone. *Carbohydr. Polym.* **80**, 1028–1036 (2010).
52. Lv, Q., Wu, M. & Shen, Y. Enhanced swelling ratio and water retention capacity for novel super-absorbent hydrogel. *Colloids Surf. A Physicochem. Eng. Asp.* **583**, 123972 (2019).
53. Dirks, J.-H. Physical principles of fluid-mediated insect attachment - shouldn't insects slip? *Beilstein J. Nanotechnol.* **5**, 1160–1166 (2014).
54. Lee, Y. S. et al. A biodegradable bioinspired oil-coated adhesive film for enhanced wet adhesion. *Surf. Interfaces* **35**, 102415 (2022).
55. Hwang, G. W., Lee, H. J., Kim, D. W., Yang, T.-H. & Pang, C. Soft microdenticles on artificial octopus sucker enable extraordinary adaptability and wet adhesion on diverse nonflat surfaces. *Adv. Sci.* **9**, e2202978 (2022).
56. Lee, Y. S., Kang, G. R., Kim, M.-S., Kim, D. W. & Pang, C. Softened double-layer octopus-like adhesive with high adaptability for enhanced dynamic dry and wet adhesion. *Chem. Eng. J.* **468**, 143792 (2023).
57. Tan, X., Guo, D. & Luo, J. Different directional energy dissipation of heterogeneous polymers in bimodal atomic force microscopy. *RSC Adv.* **9**, 27464–27474 (2019).
58. Galassi, T. V. et al. Long-term in vivo biocompatibility of single-walled carbon nanotubes. *PLoS ONE* **15**, e0226791 (2020).
59. Hou, Y. et al. A fast UV-curable PU-PAAm hydrogel with mechanical flexibility and self-adhesion for wound healing. *RSC Adv.* **10**, 4907–4915 (2020).
60. Martín, A. et al. Epidermal microfluidic electrochemical detection system: enhanced sweat sampling and metabolite detection. *ACS Sens* **2**, 1860–1868 (2017).
61. Sekine, Y. et al. A fluorometric skin-interfaced microfluidic device and smartphone imaging module for in situ quantitative analysis of sweat chemistry. *Lab Chip* **18**, 2178–2186 (2018).
62. Choi, J. et al. Soft, skin-integrated multifunctional microfluidic systems for accurate colorimetric analysis of sweat biomarkers and temperature. *ACS Sens.* **4**, 379–388 (2019).
63. Song, Y. et al. Wireless battery-free wearable sweat sensor powered by human motion. *Sci. Adv.* **6**, eaay9842 (2020).
64. Zhang, K., Zhang, J., Wang, F. & Kong, D. Stretchable and super-wettable colorimetric sensing patch for epidermal collection and analysis of sweat. *ACS Sens.* **6**, 2261–2269 (2021).
65. Mogera, U. et al. Wearable plasmonic paper-based microfluidics for continuous sweat analysis. *Sci. Adv.* **8**, eabn1736 (2022).
66. Wang, M. et al. A wearable electrochemical biosensor for the monitoring of metabolites and nutrients. *Nat. Biomed. Eng.* **6**, 1225–1235 (2022).
67. Yue, X. et al. Simple, skin-attachable, and multifunctional colorimetric sweat sensor. *ACS Sens.* **7**, 2198–2208 (2022).
68. Ye, C. et al. A wearable aptamer nanobiosensor for non-invasive female hormone monitoring. *Nat. Nanotechnol.* **19**, 330–337 (2024).
69. Frank, K. et al. Relationship between forehead motion and the shape of forehead lines—a 3D skin displacement vector analysis. *J. Cosmet. Dermatol.* **18**, 1224–1229 (2019).
70. Patterson, M. J. et al. Variations in regional sweat composition in normal human males. *Exp. Physiol.* **85**, 869–875 (2000).
71. Leiper, J. B. et al. Comparison of water turnover rates in men under taking prolonged cycling exercise and sedentary men. *Int. J. Sports Med.* **22**, 181–185 (2001).
72. Zhao, J. et al. A wearable nutrition tracker. *Adv. Mater.* **33**, 2006444 (2021).

Acknowledgements

This research was supported by National Research Foundation (NRF) grants funded by the Korean government (MSIT): 2022R1A4A3032923 (C.P. and S.-Y.C.), RS-2023-00211580 (S.-Y.C.), and RS-2024-00352352 (C.P.). This research was also supported by the Ministry of Health & Welfare, Republic of Korea (HP23C001100, S.-Y.C.), and a National Research Council of Science & Technology (NST) grant from the Korean government (MSIT) (CRC23021-000, C.P.).

Author contributions

Y.S.L, S.S., S.-Y.C., and C.P. conceived the idea and designed the project. Y.S.L. and S.S. conducted experiments with the assistance of G.R.K., S.L., and D.W.K. supported the drainage and adhesion modeling calculations. S.P., Y.C., S.H.J., and D.L. assisted the *on-body* sweat test. Y.S.L, S.S., S.-Y.C., and C.P. wrote the manuscript with input from all the authors. All authors contributed to discussions informing the research.

Competing interests

The authors declare no competing interests.

Additional information

Supplementary information The online version contains supplementary material available at https://doi.org/10.1038/s41467-025-58425-x.

Correspondence and requests for materials should be addressed to Soo-Yeon Cho or Changhyun Pang.

Peer review information *Nature Communications* thanks Giovanni Salvatore and the other anonymous reviewer(s) for their contribution to the peer review of this work. A peer review file is available.